Biomimetic plasmonic nanophages by head/tail self-assembling: gold nanoparticle/virus interactions

Hazem Ahmed [a], *Hender Lopez* [b], *Francesco Boselli* [c,d], *Giulia Tarricone* [a], *Silvia Vercellino* [e], *Paolo Emidio Costantini* [f], *Valentina Castagnola* [e,g], *Marina Veronesi* [h], *Fabio Benfenati* [e,g], *Alberto Danielli* [f], *Luca Boselli* [a*], *and Pier Paolo Pompa* [a*]

[a] Nanobiointeractions&Nanodiagnostics Lab, Istituto Italiano di Tecnologia, Via Morego 30, Genova 16163, Italy.

[b] School of Physics, Clinical and Optometric Sciences, Technological University Dublin, Grangegorman D07 ADY7, Ireland.

[c] Department of Biosciences, Durham University, South Road, Durham DH1 3LE, United Kingdom.

[d] Department of Engineering, Durham University, South Road, Durham, DH1 3LE, United Kingdom.

[e] Center for Synaptic Neuroscience and Technology, Istituto Italiano di Tecnologia, Largo Rosanna Benzi 10, Genova 16132, Italy.

[f] Dipartimento di Farmacia e Biotecnologie, Alma Mater Studiorum Università di Bologna, Via Francesco Selmi 3, Bologna 40126, Italy.

[g] IRCCS Ospedale Policlinico San Martino Largo Rosanna Benzi 10, Genova 16132, Italy.

[h] Structural Biophysics Lab, Istituto Italiano di Tecnologia, Via Morego 30, Genova 16163, Italy.

ABSTRACT

Gold nanoparticles (AuNPs), thanks to their dual plasmonic and catalytic functionalities, are among the most promising nanomaterials for the development of therapeutic and diagnostic tools for severe diseases such as cancer and neurodegeneration. Bacteriophages, massively present in human biofluids, are emerging as revolutionary biotechnological tools, as they can be engineered to display multiple specific binding moieties, providing effective targeting ability, high stability, low cost, and sustainable production. Coupling AuNP with phages can lead to an advanced generation of nanotools with great potential for biomedical applications. In the present study, we analyzed the interactions between differently sized AuNPs and filamentous M13 phages, establishing an advanced characterization platform that combines analytical techniques and computational models for an in-depth understanding of these hybrid self-assembling systems. A precise and structurally specific interaction of the AuNPs-M13 hybrid complexes was observed, leading to a peculiar head/tail "tadpole-like" configuration. *In-silico* simulations allowed explaining the mechanisms underlying the preferential assembly route and providing information on AuNPs' size-dependent interplay with specific M13 capsid proteins. The AuNPs-M13 structures were proven to be biomimetic, eluding the formation of biomolecular corona. By keeping the biological identity of the virion, hybrid nanostructures maintained their natural recognition/targeting ability even in the presence of biomolecular crowding. In addition, we were able to tune the hybrid nanostructures' tropism towards *E. coli* based on the AuNPs size. Overall, our results set the fundamental basis and a standard workflow for the development of phage-based targeting nanotools, valuable for a wide spectrum of nanotechnology applications.

KEYWORDS: M13 bacteriophages, gold nanoparticles, bio-nano interactions, biomolecular corona, nanomedicine, plasmonic nanohybrids, self-assembly

Nanotools with controlled biological identity and capability to recognize and be recognized in biological fluids are in great demand, since their targeting ability could be exploited for sensing/diagnostic and pharmaceutical applications.

M13 bacteriophages, filamentous viruses (about 1 μm in length) which exclusively infect bacteria, are emerging as sustainable biological probes in this context. Unlike most monoclonal antibodies, M13 phages are very stable and durable, and their production from bacteria is highly cost-effective, and avoid the use of animals.[1-4] M13's filamentous structures (which present a high aspect ratio) are quite monodisperse in size, presenting a precise biomolecular composition. Despite their length, the width of only 5-7 nm, which is similar to the size of antibodies recognition part, allows for similar spatial binding resolution. M13 presents a malleable nature and can undergo chemical modifications[3] and genetic engineering (i.e., *via* "phage display"[5]) of the minor protein coat pIII (the tip of the vector) and of the major protein coat pVIII (covering the lateral surface of the vector) orthogonally. This allows the definition of different targeting designs displaying binding moieties, such as single chain and single domain antibodies (scFv, sdAb or nanobodies), ligands, or peptides that can provide specificity, avidity, and affinity for a target of interest.[6, 7] Phages are already naturally present in the human body (the so-called phageome),[8] mainly in the gut, but they can also be largely found in biofluids such as saliva and urine[9]; more recently, they were detected also in peripheral blood in lower concentration, a phenomenon that was attributed to translocation of phages across cells.[10, 11]

Despite their great targeting ability and stability in complex biological environments[12, 13] there is still much to be explored to maximize the biotechnological potential of phages. For instance, engineered M13 viral particles are under consideration for their applications in immune assays devices (coupled with dyes or peroxidase enzymes) and for the treatment of bacterial infections and cancer (for example functionalized with photosensitizers for photodynamic approaches).[14-18] Nevertheless, it must be stressed that M13 characterization is not trivial, and that the molecular structures of M13 and derived phages (especially if engineered) still require fundamental research.[19] For this reason, despite being studied for some years, phage-based therapy research is still in its infancy.

Coupling the physical-chemical properties of NPs with phages can lead to the generation of active nanotools with great sensing, therapeutic, and imaging potential, presenting high sensitivity and efficacy.[20-26] The idea behind the use of such hybrid systems entails the introduction of a paradigm for M13, employing the "whole virus" as a scaffold or a biological targeting unit instead of exploiting phages exclusively to produce and isolate a moiety of interest, as it is done in the classic phage display.[5, 27, 28] A few bioconjugation strategies involving different chemical approaches have been attempted using cross-linking chemistry and engineered peptides.[28-30]

Gold nanoparticles (AuNPs) represent one of the most used nanomaterials due to the precise control gained over their synthetic process and their exploitable physical/chemical features.[31] Thanks to their size, shape, surface chemistry tunability,[32-34] optical properties (based on the localized surface plasmon resonance - LSPR),[34] and catalytic/enzyme-like[35-37] properties, AuNPs are among the most promising nanomaterials in nanomedicine, for both therapeutics (*i.e.,* drug delivery and photothermal therapy) and diagnostics (*i.e.,* already in use in commercial lateral flow immuno-assays), where they are commonly employed coupled to antibodies.[35, 38-42] Some recent explorative examples combining AuNPs and phages (often involving thiolation of the phage surface) have shown the great potential of these hybrid plasmonic systems in the field.[30, 43, 44] However, much has still to be done concerning the characterization of these types of nanotools, which needs to be systematically addressed, especially considering the lack of cognition pertaining the spontaneous interactions of NPs with phages. Unlocking the fundamental parameters governing the bio-nano interactions of AuNPs with M13 phages would inevitably promote a broad range of different applications. In the present work, we investigated the potential of the self-assembly strategy to obtain biomimetic AuNPs-M13 hybrid systems. For this study, we have implemented an advanced characterization platform that includes a large panel of complementary techniques, mathematical models for data interpretation, and *in silico* simulations. The detailed analysis of AuNP-M13 interactions allowed us to understand and control the self-assembly process, which led to geometrically precise binding, with peculiar "tadpole-like" hybrid nanostructures. *In silico* modelling coupled with immunoassays and plaque assays disclosed interesting insights about the specific protein residues involved in the formation of the AuNP-M13 complexes and revealed an AuNP size-dependent influence on the virion natural tropism. Interestingly, the plasmonic hybrid complexes exhibited high stability and biomimetic behavior in complex biological fluids (protein-rich environment), eluding the formation of a long-lasting biomolecular corona and keeping the virion bio-identity recognizable, which represents a valuable asset in view of therapeutic applications. Altogether, this study led to a profound understanding of these systems as a potential breakthrough for their future applications in nanomedicine.

RESULTS

Building blocks characterization

Citrate-capped AuNPs represent the first building block of our hybrid system. Different AuNPs (5, 15, and 50 nm of diameter) were selected to explore a potential size effect in the interactions with M13 phages. The AuNP colloidal suspensions present a strong light absorption in the visible range (LSPR band), very sensitive to their aggregation state and protein adsorption (dielectric changes at the NP interface can lead to an LSPR shift); these properties were exploited to characterize their interactions with M13.

Citrate was chosen as the capping agent since it is a small molecule (minimal steric hindrance) and a mild stabilizing agent, allowing for strong NP-biomolecule interactions. Whereas the 5 and 15 nm AuNPs were synthesized by the modified Turkevich-Frens method,[39, 45, 46] for the 50 nm we adopted a seed-mediated growth method to better control the particle size and shape distribution, using a slight modification of a previously reported method (see Methods in Supporting Information). [39]

The AuNPs were characterized by transmission electron microscopy (TEM) (**Figure 1A-D**), dynamic light scattering (DLS) (**Figure 1E**), and UV-Vis absorption spectroscopy (**Figure 1F),** showing highly monodisperse samples with expected sizes confirmed by all techniques.

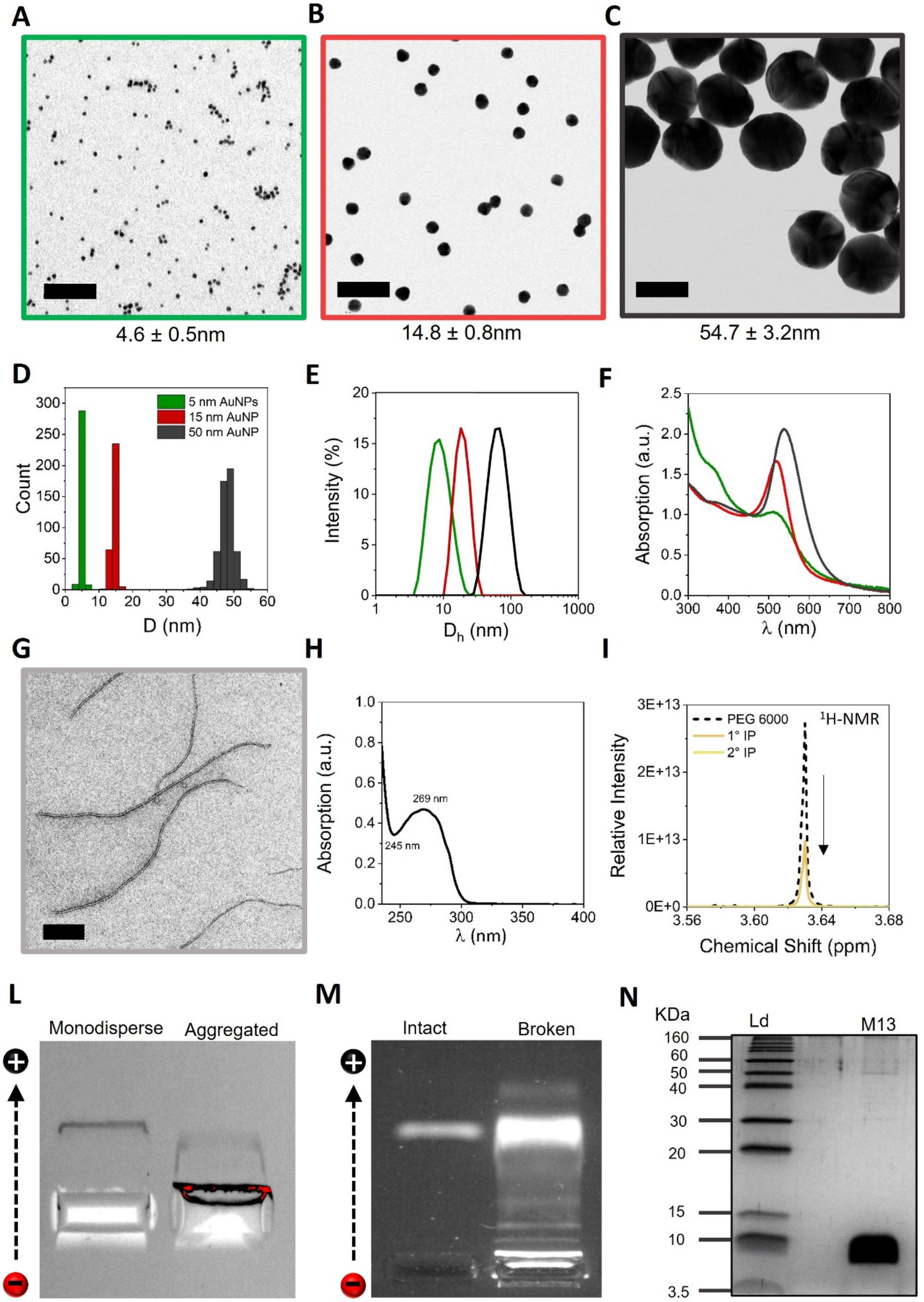
A
B
C
4.6 ± 0.5nm
14.8 ± 0.8nm
54.7 ± 3.2nm
D
5 nm AuNPs
15 nm AuNP
50 nm AuNP
Count
D (nm)
E
Intensity (%)
D_h (nm)
F
Absorption (a.u.)
λ (nm)
G
H
269 nm
245 nm
Absorption (a.u.)
λ (nm)
I
PEG 6000
1° IP
2° IP
^{1}H-NMR
Relative Intensity
Chemical Shift (ppm)
L
Monodisperse
Aggregated
M
Intact
Broken
N
KDa
Ld
M13
160
60
50
40
30
20
15
10
3.5

Figure 1. Characterization of the building blocks. Representative TEM micrographs of **A)** 5 nm AuNPs, **B)** 15 nm AuNPs and **C)** 50 nm AuNPs; **D)** histograms of the corresponding TEM size distribution showing the average diameter; **E)** Dynamic light scattering (DLS) analysis of the AuNPs library (by Intensity percentage) showing the related hydrodynamic diameter (D_h) distributions and **F)** UV-Vis spectra (normalized at 450 nm) showing the characteristic LSPR maxima (5 nm AuNPs - λ_{max}=509 nm; 15 nm AuNPs - λ_{max}= 519 nm; 50 nm AuNPs - λ_{max}=537 nm). **G)** Representative TEM micrograph of wild-type M13 bacteriophage (scale bar: 50 nm); **H)** M13 phages characteristic UV spectrum. **I)** ^{1}H NMR spectra of the M13s validating the removal of PEG 6000 content: non purified (dashed curve), purified via 1 isoelectric point (solid orange curve) and 2 isoelectric point (yellow curve), **J)** 2.5% agarose gel-assay carried in native buffer (pH= 8.4) and ran for 50 min at 90 V, showing the different electrophoretic mobility and the colloidal stability of pure (monodispersed) (lane 1) and non purified (lane 2) M13 phages; **K)** SYBR gold stained 2% agarose gel electrophoresis, carried in Tris-Borate-EDTA buffer (pH = 8.3) and ran for 30 min at 90 V, loaded with purified M13 phage (lane 1) and with a boiled M13 sample, exhibiting higher free DNA debris content (lane 2 – control). **L)** 14% SDS PAGE of pure M13 showing the absence of free protein debris. On the left the molecular mass ladder (Ld).

For the second building block, the M13 wild-type (WT) phage production was performed as previously reported *via* helper phage infection of *E. coli*.[14, 15, 47] The characterization of the M13 phages is reported in **Figure 1G-N**. Special care was employed for M13 purification. In addition to the most commonly employed polyethylene glycol (PEG)-induced precipitation, used to isolate the M13 virions from bacterial debris, we adopted multiple steps (at least two) of the isoelectric point (IEP) precipitation method.[48-50] Acidifying the M13 suspension to the pH corresponding to their isoelectric point (pH = 4.2), phage flocculation occurs, allowing their separation via centrifugation from molecular contaminants, including the residual PEG otherwise massively present in the sample solution. As a final purification step, a gentle buffer exchange approach via size exclusion chromatography was employed.

Notably, undesired by-products, such as free DNA, protein debris, and PEG, can potentially adsorb onto the AuNP and M13 surface, hampering the individual reactivity of the building blocks and thus interfering with the AuNP-M13 interaction.[31, 48] An in-depth assessment of the M13 quality is fundamental for meaningful and reproducible studies, as it is necessary to exclude the presence of impurities. Therefore, the M13 structure integrity was also verified since sometimes it could be compromised by the centrifugation step or an excessive acidification of the solution during IEP steps. By employing water-suppressing ^{1}H-NMR (**Figure 1I**), we were able to detect and quantify the PEG contamination in the sample and verify its efficient removal after the purification steps (estimated PEG content < 0.1 molecule / virion).

The M13 structural integrity was verified by TEM (**Figures 1G, S1**), showing the characteristic filamentous structure of the expected size (900 nm in length and 6 nm in width). Eventually, the purity of phage preparations was also assessed by absorption spectroscopy. As reported elsewhere[51, 52], a pure M13 sample exhibits a characteristic absorption spectrum in the UV region (**Figure 1l**), with a single broad peak (245-320 nm) centered at 269 nm, due to the absorbances of M13 proteins and DNA components (a maximum centered at a shorter wavelength would suggest phage degradation). The high ratio between the maximum and minimum absorbance (A_{269}/A_{245} = 1.37) and the low baseline to max ratio (A_{350}/A_{269} = 0.02) indicate an excellent purity of the product and a good dispersibility of the M13 virions (stable colloidal suspension), whose concentration was estimated by the absorption spectrum (see Supporting Information for details).

Additionally, we analyzed the phage preparation via gel-shift assay. Interestingly, M13 can orient under the mild electric field employed and run into the agarose gel prepared in native buffer (pH = 8.4), thanks to its net negative charge. Gel electrophoresis showed a monodisperse size distribution and the absence of M13 fragments or aggregates (presenting faster and slower electrophoretic mobility, respectively) (**Figure 1L**). The potential presence of free DNA residues was excluded by employing DNA staining agarose gel assay (**Figure 1M**) and further analysis with polyacrylamide gel electrophoresis (SDS-PAGE) showed the absence of free-protein contaminants (**Figure 1N**), while clearly showing the M13 related major coat protein pVIII band migrating at ~ 6-10 KDa.

Finally, M13 integrity was further validated by a plaque assay, showing that the majority of virions withheld infectivity (**Figure S2**). Overall, the implemented characterization platform allowed to validate the integrity and quality of the building blocks.

AuNP-M13 interactions

M13 phages comprise 2,700 copies of the pVIII coat protein on their capsids and five copies each of the minor proteins pIX and pIII located at the extremities of the filamentous structure, with pIII serving as the recognition moiety binding to the F pilus of *E. coli* host strains.

In general, proteins are known to interact and strongly adsorb onto the surface of AuNPs (*i.e.,* biomolecular corona formation) with an adsorption energy that is NP size dependent.[31, 45] However, NP interactions with this kind of filamentous virus are still poorly explored and, considering the peculiar size ratio and structural conformation of phages, the outcomes are hard to predict. When looking for the optimum reaction medium, we had to ensure maintaining the colloidal stability of both AuNPs and M13 virions, keeping a certain degree of repulsion among the individual building blocks (i.e. NP-NP and M13-M13) while facilitating their bio-nano interaction (NP-M13). After screening different reaction media (and pH), sodium citrate saline buffer (SCS – pH = 7) was selected (**Figure S3**).

It is well-established that an excess of proteins promotes the formation of the NP bimolecular corona, which commonly occurs very rapidly (within seconds in some case).[31, 45, 53-56] However, NPs are typically larger than the biomolecules adsorbing onto their surface, while in this case they are smaller than the whole M13 viral scaffold. Nevertheless, temperature- and concentration-dependent bio-kinetic processes would still govern the physical principles behind the AuNP-M13 interactions. Thus, AuNPs and M13s were incubated at various temperatures, concentrations, and reaction stoichiometries to optimize these interactions (more details are given in the following section). The analysis of the sample via TEM, DLS, UV-Vis, and SDS-PAGE was performed on isolated products (*i.e.*, after purification via centrifugation, see Methods in Supporting Information). The analysis *via* high-resolution analytical centrifuge (differential centrifugal sedimentation, HR-DCS) were instead performed *in situ* before the purification process.

Considering the different densities of the species present in the sample (free-M13, free AuNP, and AuNP-M13), the hybrid compounds made with different selected stoichiometries were isolated by an *ad-hoc* centrifugation-based protocol (see Methods and Supporting Information) and analyzed by TEM (**Figure 2**). Interestingly, all the reaction conditions tested led to a specific interaction of the AuNPs with the tip of M13 phage, obtaining a AuNP-phage head-tail configuration for all the different sizes of AuNPs employed. It is striking how orthogonal the self-assembly occurred despite the absence of any M13 engineering (no gold-binding peptides nor chemical functionalization with thiol groups). Some exceptions were observed when working with AuNP excess. In the latter case, a NP could also be found on the phage body (pVIII), but still only in addition to the one present on the tip (**Figure S4**). Primarily, the AuNPs did not tend to anchor onto the pVIII despite it represents 95% in weight of the total phage mass and, thus, almost the totality of the bio-surface available. Such strong preferential interaction for the minor coat (one of the two tips - pIII or pIX) is striking, and otherwise expected only when obtained by orthogonal chemistry involving specially prepared ligands (or M13 functionalization).

From TEM imaging of the AuNPs-M13 complex with different stoichiometries (**Figure 2**), distinct configurations were observed when 50 and 15 nm AuNP were used, from the 1:1 to multi-tail configuration.

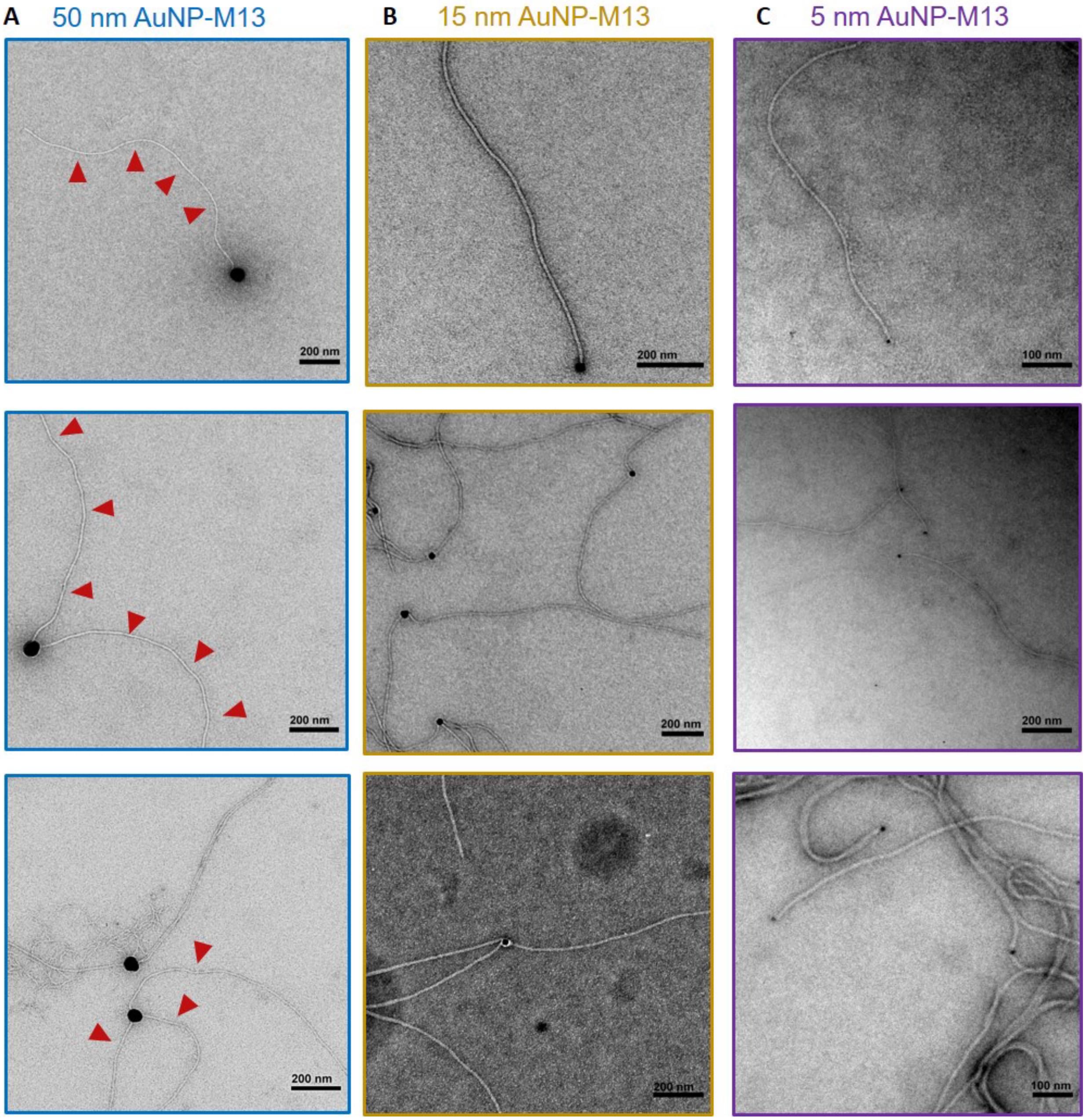

Figure 2. TEM characterization of the AuNPs-M13 interaction. Representative TEM micrographs of the predominant head-tail structures of the isolated AuNPs-M13 complexes using **A)** 50 nm, **B)** 15 nm, and **C)** 5 nm AuNPs showing the different configurations. Increasing the M13 excess (from top to bottom panels), the predominant configuration passed from 1:1 head-tail to multi-tail systems.

On top of the stoichiometry, the number of M13 tails per AuNP depended on the size of the particle: in the case of 5 nm AuNPs, the 1:1 configuration was the main complex observed even when using M13 excess, likely due to the smaller surface area available.

The absorption spectra of the purified samples were recorded and compared with respective controls (**Figure S5**). The curves exhibited the contribution of the M13 UV absorption (at 269 nm) and a red-shift of the AuNP LSPR maxima due to the interactions at the surface with M13, which, however, becomes less noticeable by increasing the AuNP size. This is in line with the head-tail complex configuration observed by TEM, indeed, the small diameter of the M13 (6 nm) interacts with a low percentage of the total 50 nm AuNP surface area (7850 nm^2); thus, a negligible change in the dielectric layer is expected when one or few phage tails are involved. Additionally, the DLS measurements (**Figure S6)** confirmed the AuNP-M13 interactions, showing a significant increase in the hydrodynamic diameter (related slow-down of the diffusion rate) compared with the AuNP control. The protein content analysis via SDS-PAGE showed one intense band at 6-10 KDa corresponding to the pVIII major coat protein and thus of the M13 phage bonded to the AuNPs (see **Figure S7**). Finally, we also confirmed the preservation of M13 structure after exposure to AuNPs by DNA-stained agarose gel analysis, excluding otherwise disruptive interactions under the selected conditions (**Figure S8**).

AuNP-M13 advanced DCS analysis exploiting a predictive mathematical model

DCS provides a distribution of the apparent size *D* of the complexes in solution, based on their centrifugal sedimentation time *T*. In this study DCS allowed for accurate high-resolution *in situ* characterization of the AuNP-M13 interactions.

By analyzing AuNPs incubated with M13 virions, we observed, in all the samples, a decrease of the AuNPs peak and the formation of one or more populations with a smaller apparent size, confirming a substantial amount of complexes formed under all the tested conditions (see **Figure 3A** for the case of 50 nm AuNP). This is in line with what was previously observed for the biomolecular corona of NPs.[57, 58] The lower density of the M13 anchored to the AuNPs leads to a longer sedimentation time because of reduced density and increased viscous friction, translating into a smaller apparent size as the instrument's direct readout.

AuNPs readily associated with M13 virions under the selected conditions (**Figure S9**). By monitoring the decrease of the DCS intensity peak related to free AuNPs (concomitant to the formation of the AuNP-M13 complexes), we could observe that, at a fixed stoichiometry, increasing the total concentrations of the reagents and temperature (37 *vs*. 23 °C) led to an increase of the building blocks association (**Figure S9**). In addition, we observed that working with an excess of M13 favored the formation of AuNP-M13 complexes more than an excess of AuNP (**Figure S9**).

To clearly understand the interaction dynamics and the complex assembly in solution with statistical relevance, we analyzed the DCS raw data (providing light extinction and sedimentation time) using a mathematical model that allowed us to predict the difference in sedimentation time of the different hybrid complexes, such as 1 head:1 tail, 1 head:2 tails, 1 head:3 tails, 1 head:4 tails (**Figure 3A-B**). This approach is reminiscent of the DCS core-shell models previously developed for NP-protein interactions[57, 59] that however is strictly valid for spherical constructs and cannot account for the slender geometry of the M13. Therefore, we developed an *ad-hoc* model to calculate the sedimentation times of AuNP-M13 hybrid systems made of N_0 particles and N_f filaments. We estimated their average velocity as $U = F/c$, where we have balanced the total centrifugal force $F = N_0F_0 + N_fF_f$ and the viscous fluid force Uc, where $c = N_0c_0 + N_fc_f$ is the friction (or drag) coefficient, and subscripts 0 and f denote the particle and phage filament contribution, respectively. For a spherical NP of diameter d_0, we used the classic Stokes coefficient $c_0 = 3\pi\mu d_0$. Excellent data fitting was obtained by modelling the M13 phage as isotropically oriented, slender filaments of length L and diameter d_f, with c_f computed as the average of the tangential and orthogonal Taylor coefficients originally derived for sperm flagella, under the assumption $\epsilon = d_f/L \ll 1$:

$$c_f = \frac{2\pi\mu L}{ln(4\epsilon^{-2}) - 1} + \frac{4\pi\mu L}{\ln(4\epsilon^{-2}) + 1}$$

The running time relative to the NPs is the inverse U_0/U of the relative terminal velocity:

$$\frac{T}{T_0} = \frac{F_0}{F}\frac{N_fc_f + N_0c_0}{c_0}$$

The peaks observed in the data correspond to $N_f = 1,2,3,4$, and $N_0 = 1,2$, and introducing the variability of the particle diameter is sufficient to explain the distribution of sedimentation times produced by the instrument.

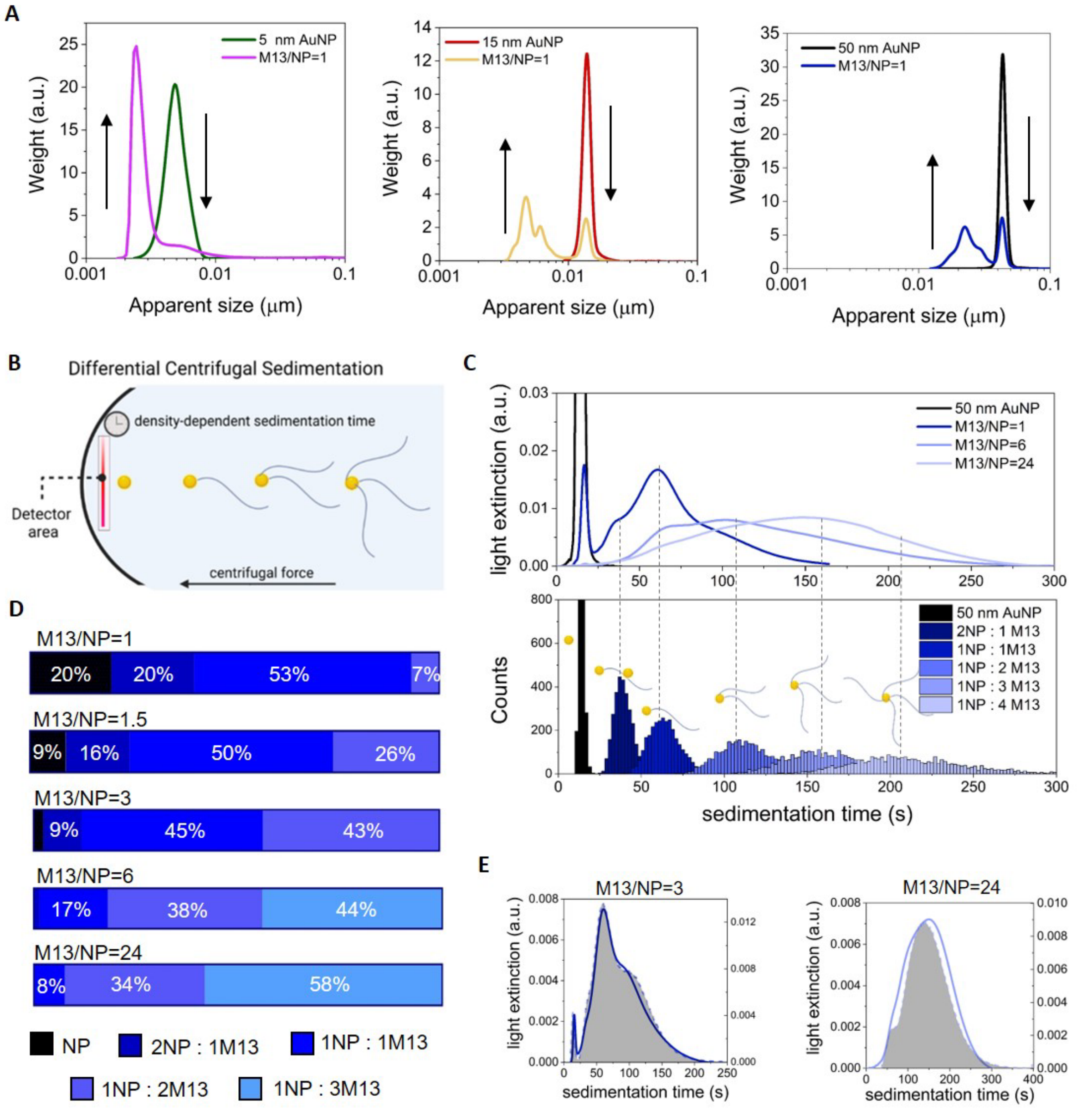

Figure 3. DCS analysis and predictive model of the different AuNP-M13 configurations. A) DCS standard measurements (in Weight) of AuNP alone and AuNP incubated with M13 for 5, 15, and 50 nm AuNPs (stoichiometry 1:1). The AuNPs present the expected sizes. The formation of AuNP-M13 complexes is testified by the presence of the peak at a smaller apparent size, due to the lower total density, and of the adducts' anisotropic shape. **B)** Schematics of the DCS analysis process: the larger the number of tails, the larger the time necessary for AuNP-M13 complexes to

reach the detector under an established centrifugal force (sedimentation time). **C-E)** Representative example of 50 AuNPs-M13 DCS analysis data fitting. **C)** The top figure represents an AuNP titration with increasing M13 concentrations (only a few curves are displayed for clarity). The bottom figure shows the AuNP-M13s sedimentation time distributions predicted by the mathematical model. **D)** Mathematical extrapolation of the AuNP-M13 populations obtained by fitting the DCS experimental curves related to the titration experiment. **E)** DCS experimental curves overlap to the computationally simulated curves. This fitting allows to identify and estimate a relative quantification of the AuNPs-M13 present in the sample.

We calculated how the complexes distributions for the 50 and 15 nm AuNPs with 1, 2, 3, and 4 tails should appear in the DCS analysis (**Figures 3C-E and S10, S11)**. The simulated peaks in **Figure 3C**, obtained considering the size distribution of the AuNP and an average M13 length of 900 nm, exhibit striking overlaps with the main experimentally observed peaks. The complexes appear with an increasing delay (larger sedimentation time) by increasing the number of M13 tails. It is useful to mention that, since the width of a distribution of values increases when each of its individual values is multiplied by a positive constant, it is logical to observe that also the AuNP-M13 peak variance increases with increasing numbers of M13. This also means that we cannot compare the amount of one population with another by simply comparing their peak intensities.
The complete titrations performed for 50 and 15 nm AuNPs accompanied with representative TEM micrographs related to the main populations are reported in the Supporting Information (**Figures S10-S12**). The measurement for the 5 nm AuNP-M13 complexes resulted at the instrumental resolution limit (and near the limit of detection); thus, titration was not performed in this latter case.

The model allowed us to identify and quantify the relative abundance (%) of the complex configurations obtained by varying the M13/AuNP reaction stoichiometry in a quite precise way when simulating the DCS peaks (excellent fit of the data, **Figure 3E and S11)**, taking into account the possible presence of AuNP-M13 mixed populations (**Figure 3D-E**). This approach overcomes the above-mentioned nonlinear relation between the peak intensities and the fraction of a complex in solution. When the free AuNP depletion and product formation curves were monitored in DCS as a function of the increasing amount of M13, we observed that the assembly occurs at stoichiometric conditions and that the adsorption becomes more efficient by increasing the M13 concentration, leading to the formation of two-tail and three-tail complexes already in the presence of less than five M13 per particle. This occurs even in the case of 15 nm AuNPs, in spite of more relevant steric hindrance effect on the reduced available surface (**Figure 3D and S13**). Overall, these data suggest a high AuNP-M13 binding affinity.

AuNP-M13 behavior in biological media

The behavior of the AuNP-M13 complexes was also tested in various media, namely in high ionic strength buffers (*e.g.,* phosphate buffer saline - PBS, **Figure S14**) and protein rich biological fluids (**Figure 4**) in view of future biomedical application. After incubation (see Methods in Supporting Information for experimental details), the complexes were analyzed by UV-Vis spectroscopy, SDS-PAGE, and DCS. Interestingly, while the citrate-stabilized AuNPs (as expected) rapidly aggregated in PBS, resulting in a broader and red-shifted spectrum of their LSPR band, the AuNP-M13 hybrids gained increasing stability with the increasing number of complexed M13 phages, until obtaining an invariant spectrum (multiple M13 tails were necessary to stabilize the larger 50 nm AuNP, **Figures S14, S15**). Therefore, AuNP-M13 complexes prepared using an excess of M13 were employed for the test in biological fluids. As shown in **Figure 4B**, the colloidal stability and dispersion of the AuNP-M13 hybrid complexes in 10% (*in vitro*-like) and 50% serum (*in vivo*-like) were proven to be unaltered with no remarkable changes in the absorption spectra. Similar results were obtained using the LB culture media (commonly used for bacterial growth, **Figure S16**).

Interestingly, DCS analysis in this context also provided information on the structural stability of the hybrid systems in the different media, since no significant biomolecular corona driven M13 displacement was observed in any of the tested conditions (**Figure 4C**). The SDS-PAGE analysis of the samples isolated after serum incubation also confirmed the invariant M13 content, indicating that biomolecular substitution did not occur (**Figure 4D**), even for the systems involving the smaller AuNPs (commonly presenting weaker adsorption). The AuNP (and M13) content in the different samples were normalized with the one of the related AuNP-M3 complex to ensure a meaningful comparison. Furthermore, these studies, involving the analysis of the protein content of the AuNP-M13 after exposure to biofluids, led us to conclude that the serum-derived protein corona formation is almost eliminated for AuNP-M13 compared to the one forming onto the pristine AuNPs (only the albumin related band at 60-70 kDa is barely visible in addition to the 8-10 kDa pVIII one: **Figures 4D, S17** and control experiments on WT-M13 in **Figure S18**). This suggests that the bacteriophage represents the main biological identity of the AuNP-M13 in complex biological fluids, which could be a significant asset for their applications in drug delivery or in diagnostics. Indeed, when aiming to control the biological identity of drug carriers in nanomedicine, the specific targeting agents are often completely masked by the biomolecules present in the biological fluids, which adsorb onto the nanocarrier surface, and consequently mask the previously prepared functionalities and hamper the recognition.[31, 55, 60]

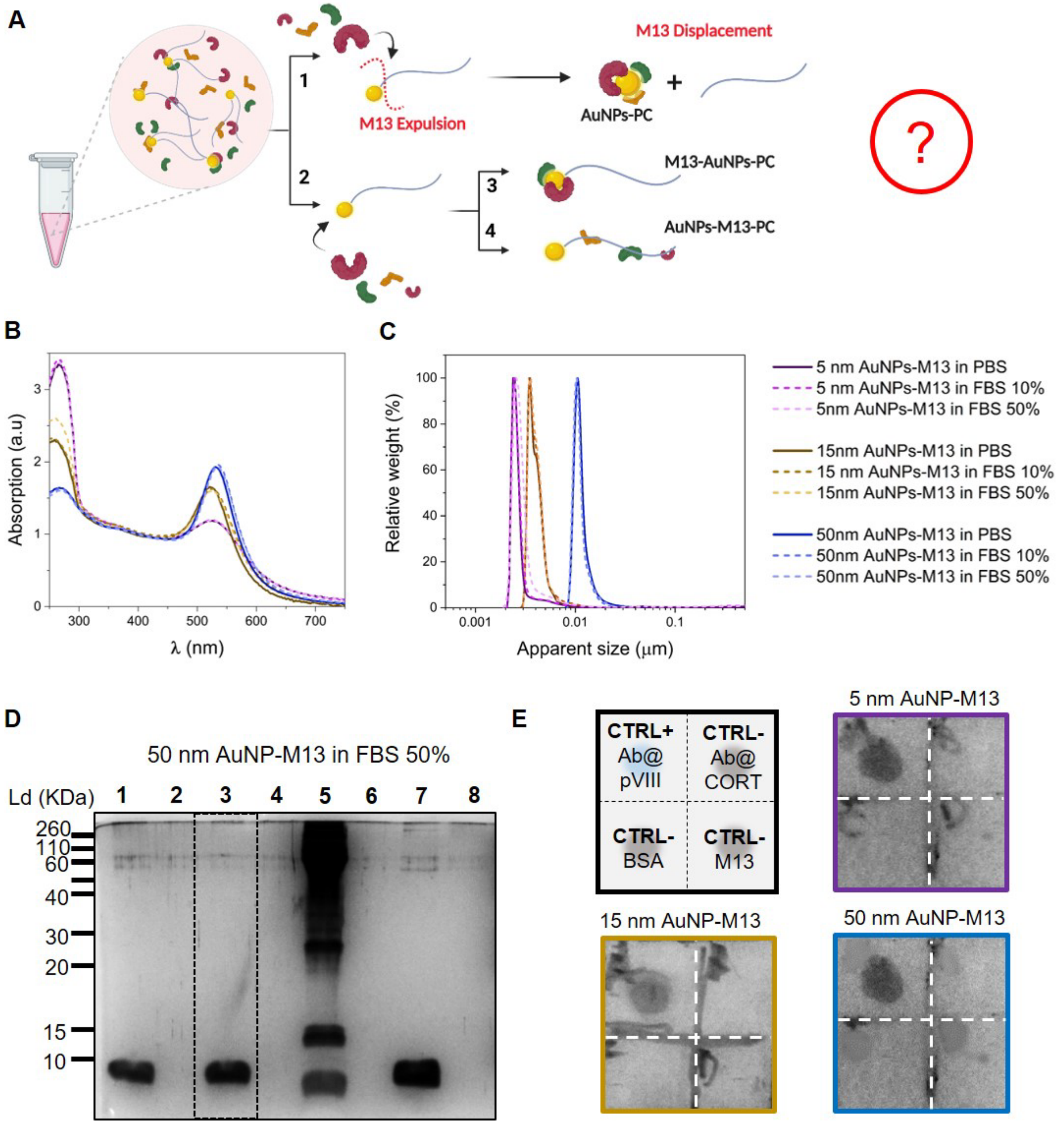

Figure 4. AuNP-M13 in biological media. A) Schematics of the AuNP-M13 in biofluid and their possible type of interactions with biomolecules: 1. Protein-mediated M13 displacement; 2. The AuNP-M13 is stable, and no further corona is formed; 3. Protein corona forms on the NP available surface of the AuNP-M13, 4. Protein corona forms on the filament. Option 3 and 4 could coexist,

leading to the formation of AuNP-M13 protein coating and potentially compromising the biological identity. **B)** UV-Vis analysis of AuNP-M13 complexes in serum. **C)** DCS analysis (in relative weight) of AuNP-M13 complexes before and after incubation with serum. **D)** SDS-PAGE analysis of the AuNP-M13 protein composition after 48 h incubation in 50% FBS: lane 1- AuNP-M13 control (not exposed to FBS), lane 3- AuNP-M13 exposed to 50% FBS, lane 5- AuNP exposed to 50% FBS (hard protein corona), lane 7- M13 exposed to 50% FBS. Lanes 2, 4, and 6 are the related wash controls. In this experiment the AuNP and the M13 concentrations (number of particle/mL) were normalized with the one in the related AuNP-M13 complex. **E)** Dot-Blots showing the AuNP-M13 recognition by antibody anti-pVIII in protein-rich media (50% serum). The spot is visible by the naked-eye thanks to the AuNP color; the Image was acquired using Gel-Doc.

We preliminary tested the recognition capability of the AuNP-M13 by anti-pVIII monoclonal antibody (**Figure 4E**), observing that the binding process was efficient even in a protein-rich environment (50% serum). In these experiments, the optical properties of AuNPs were exploited for naked-eye detection, a similar approach to the one applied in commercially available lateral flow devices (*e.g.,* Covid-19 rapid test kits). These assays suggest, in principle, the potential to translate our systems to diagnostics applications, as an alternative to antibody-based strategies.

In-silico simulations of AuNP-M13 complex formation explain the orthogonal interaction

To better understand the nature of AuNP interaction with the M13 virion, we analyzed *in-silico* their tendency to adsorb onto the different M13 components, with a particular focus on pVIII, pIII, and pIX, forming the filament body or located at the two virion tips, respectively (**Figure 5A**). For the computational simulations, we developed a coarse-grained (CG) model from a previously validated methodology used to study the adsorption of proteins onto AuNPs.[61] Briefly, the model represents the proteins at a residue level, and the protein-surface interactions are parameterized from all-atom simulations. The model also includes electrostatic and van der Waals interactions with the core material of the NP, as well as the surface chemistry contribution during the adsorption energy calculation, which has already been shown to play an important role in this context.[31, 62] For the simulations we employed the crystal structures of pIII (and part of the pVI), pVIII, and pIX M13's components (PBD ID 8b3o, PBD ID 8b3q, PBD ID 8b3p) recently reported.[19] For the pIII N-domains component, we used Alphafold2[63] to predict the protein structure using partial structures of the pIII (PDB ID 1G3P, PDB ID 2G3P)[64, 65] as templates and the sequence of the protein. Notice that the obtained structure only represents a portion of the protein, as the whole structure is composed of 5 of these elements arranged in a ring shape fashion. For this reason, we calculated and compared between them the adsorption energies of AuNP interacting with the M13 protein components, where for the pIII we considered rings of variable diameter (and orientation) built from assembling 5 single tips pIII structures **(Figure 5B-D)**. Noteworthy, our results indicated that the greatest probability of adsorption is by far for the AuNP adsorption onto pIII. Analyzing the two different contributions (electrostatic and van der Walls) to the total adsorption energy, we observed that the "molecular" driving forces that guide the binding were not much based on electrostatic interactions between the negatively charged AuNPs and the positively charged pIII residues, but mainly on van der Waals forces even for 5 nm AuNP (**Figure S19**).

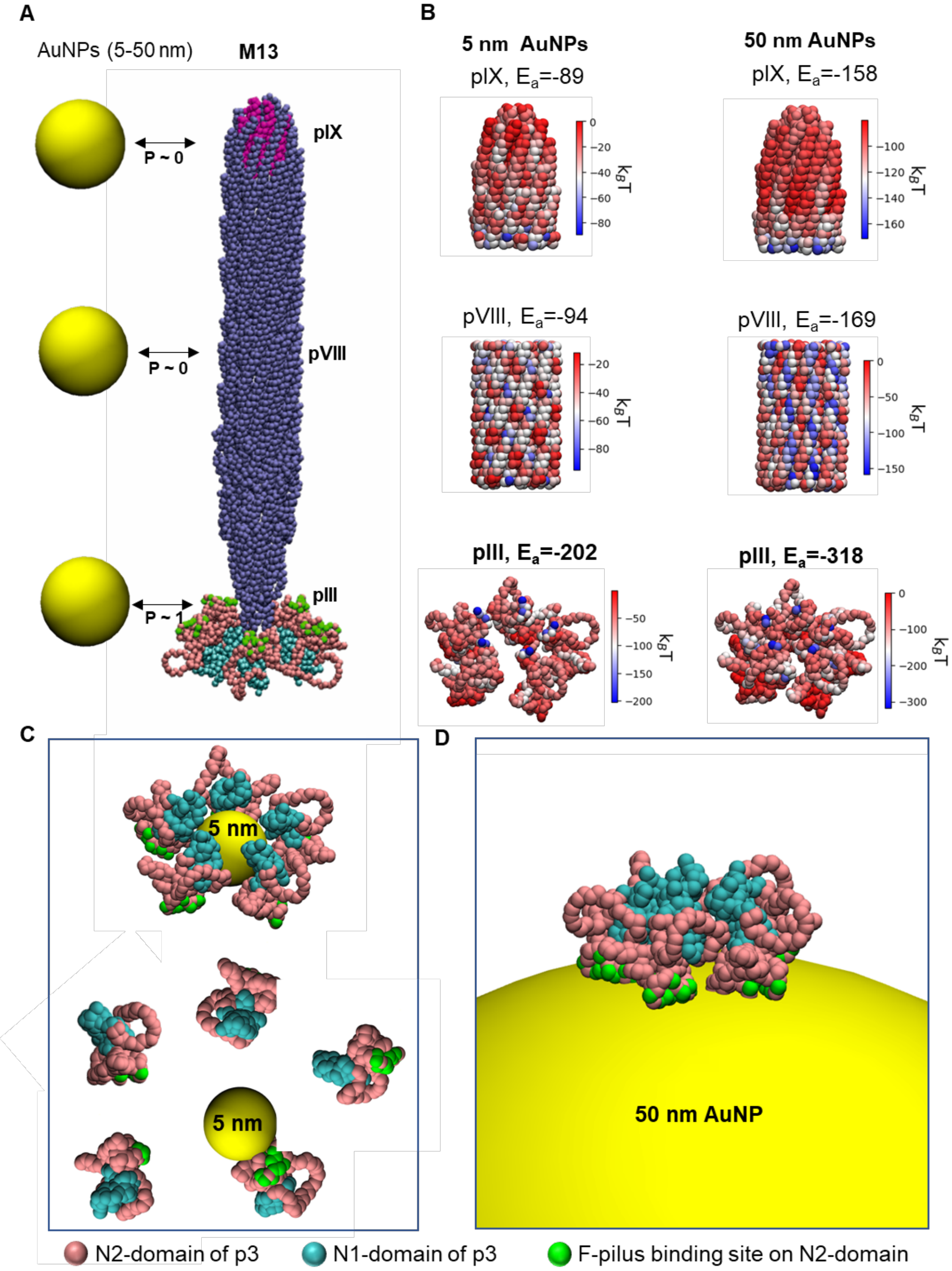

Figure 5. In silico AuNPs-M13 interaction. A) Structure of WT-M13 (with shortened pVIII) and probability of assembly in a 1 to 1 interaction with AuNPs at the different sites. **B)** Adsorption

energies calculation of AuNP are related to pIX, pVIII, and pIII. The color of the structure is a k_BT values heat map (blue color for low k_BT, red color for high k_BT). The lower the k_BT, the more important the expected interaction. This aspect influences the protein orientation during AuNP adsorption. **C)** Possible configurations for 5 nm AuNP-pIII interaction. The configuration characterized by lower energy is located on top, but considering the NPs size and the pIII component flexibility, the configuration on the bottom is also expected to occur (since it is energetically favored). **D)** Simulation of the more stable and energetically favored 50 AuNP-pIII configuration. The five pIII units are all adsorbed onto the AuNP surface.

The pIII is formed by three domains N1, N2, and C (67, 131, and 150 residues, respectively) that are separated by two flexible glycine-rich linkers (N1, N2, and the linkers are not visible at TEM, but their structures have been reported). By observing the adsorption energy variation with the pIII arrangements (*i.e.,* different distances in between the N1-N2 domains**, Figure S20**), we could assume that the strong AuNP-M13 interaction should also be related to the peculiar pIII structure and the fact that its five composing units can move, rearranging their spatial configuration with a high degree of freedom. For instance, exploring different pIII ring diameters, it is easy to observe how the pIII arrangement at the AuNP surface can significantly affect the total adsorption energy (**Figure S20**). While all AuNP sizes were shown to interact preferentially with the N2 domain, the different sizes do it in a different fashion. Indeed, while the 50 nm AuNP, due to its large available surface, can interact with all the five N2 domains simultaneously, making contacts with a large number of residues, one 5 nm AuNP could interact with only one of them, leaving the other 4 free (**Figure 5 C,D**). However, this is still the preferential interaction if compared with pVIII and pIX. Interestingly, for all AuNP sizes, *in silico*, the interaction occurred at (or in the proximity of) the

F-pilus binding site, and the interaction was stronger than the AuNP-albumin (HSA / BSA) one (**Figure S21**), which explains the high structural stability of the AuNP-M13 assemblies previously described in serum. To be more precise, for the 5 nm AuNP, the interactions with one pIII unit and HSA were comparable but considering the entropic penalty behind the replacement process and the competition of the other 4 pIII units in the close proximity, the replacement is quite unlikely to occur (at least not in the short term). Furthermore, as our pIII model is rigid, we do not account for the possibility that the size and configuration of the ring can adapt to lead to more energetically favorable arrangements that will make the replacement of the AuNP by HSA even more unlikely.

AuNP interactions with the M13-pIII can impact the natural M13 tropism in a size dependent manner

To better understand the *in-silico* results, we tried to validate the theoretical AuNP-M13 interactions at the pIII by performing additional immunoblotting tests (see Methods in Supporting Information). The complexes were spotted on a nitrocellulose membrane and the pIII availability was probed using specific primary antibodies (**Figures 6A,B** and control experiments in **Figure S22**).

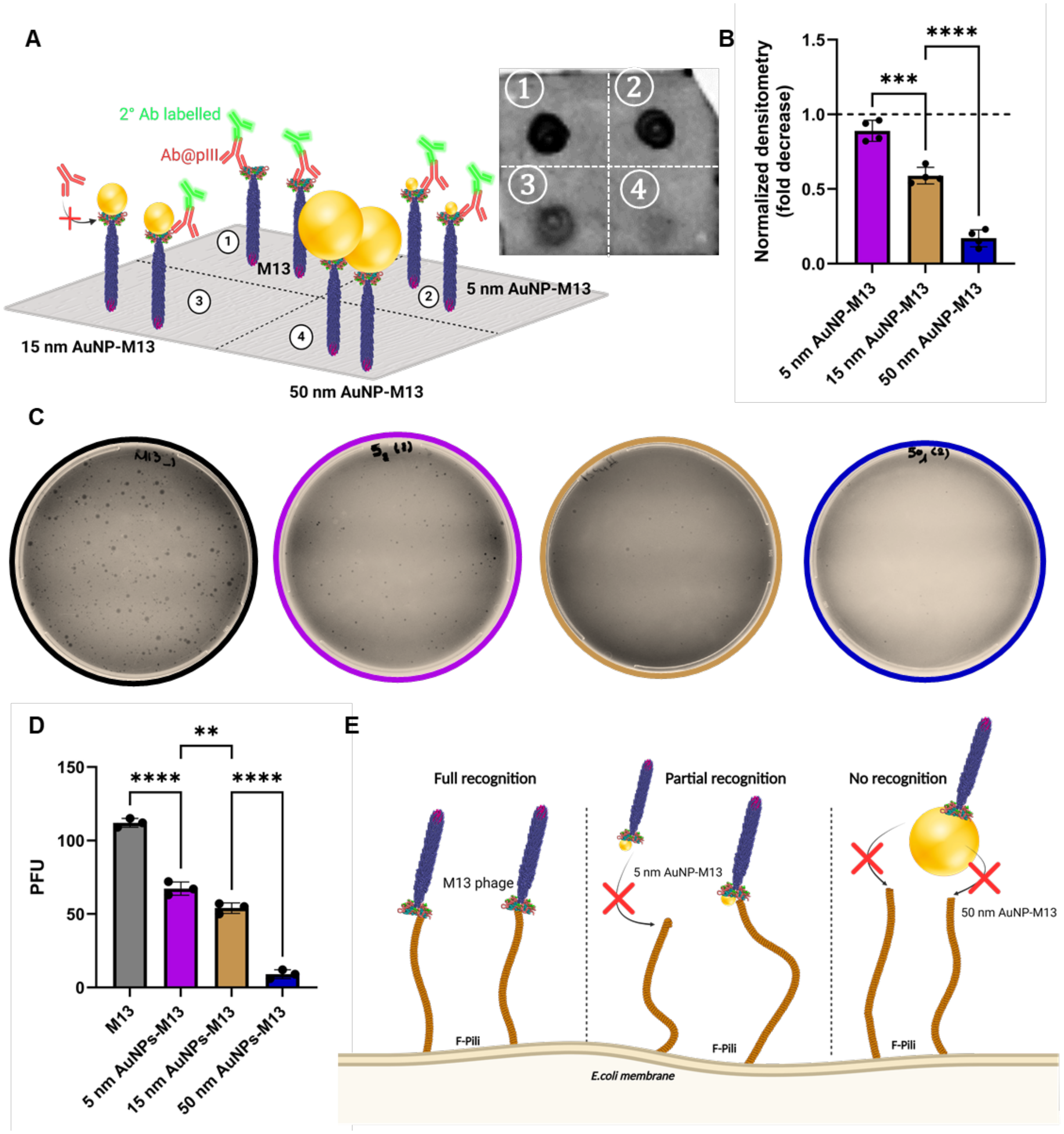

Figure 6. Biofunctional properties of the AuNP-M13 complexes and AuNP influence on M13 infectivity. A) Dot blot immunometric assay recorded in fluorescence of the pIII-recognition assessment of AuNPs-M13 library compared to free M13. **B)** Quantification of the dot blot by optical densitometry. Data are presented as average ± SD of four independent experiments

normalized over M13 control. Statistical analysis: ****$p < 0.0001$, ***$p < 0.001$, one-way ANOVA/Tukey's tests. **C)** Representative plaque assay showing AuNPs-M13 complex infectivity in *E. coli* compared to free M13. **D)** Plaque assay quantification performed by counting the number of average plaque forming units (PFU). Data are presented as average ± SD of three independent experiments. Statistical analysis: ****$p < 0.0001$, **$p < 0.01$, one-way ANOVA/Tukey's tests. **E)** Schematic illustrating the NP size-dependent behavior of the AuNP-M13 during *E. coli* infection: the 50 nm AuNP hampered the M13-pilus recognition necessary for the infection, while 5 nm AuNP only partially inhibited the engagement with the pilus.

The 50 nm AuNPs, masking the pIII completely, hamper the antibody recognition, while decreasing the NP size increased the pIII availability (and recognition). Hence, the size-dependent bio-nano interactions found *in-silico* well correlates with the experimental differences observed here, in terms of the AuNP-M13 recognition.

We further investigated this aspect, by analyzing the effect of AuNPs on the M13 natural tropism. M13 can infect *E. coli* bacteria through a sophisticated mechanism triggered by the pIII anchoring the F-pilus, a hair-like appendage composed of oligomeric fibrous proteins present on the bacterial surface.[19] However, *in-silico*, we observed that the AuNP interaction with pIII occurs at the F-pilus binding domain, which is responsible for the M13-pilus engagement.

Performing the plaque assay, we analyzed the infectivity of our AuNP-M13s in *E. coli* (**Figure 6C-E**). This test is commonly used to quantify the infective potential of M13 (as previously discussed). The larger the number of forming plaques, the larger the number of bioactive M13 virions. Interestingly, all the hybrid assemblies showed inhibition of the infectivity. However, while the 50 nm AuNP impact was striking, almost completely abolishing M13 infection, the smaller particles had a lower impact on the phage, only partially inhibiting the infection process (**Figure 6C-E**). This phenomenon is in close agreement with the above computational simulations. All the AuNPs adsorb in proximity to the pIII residue associated with the M13 recognition of the F-pilus (requisite for the M13 infection of *E. coli*). The 50 nm AuNPs, due to their large size, cover almost all these key residues for all the five pIII units (all adsorbed onto the NP surface). The situation is different for the 5 nm AuNP, whose size is similar to that of a pIII unit, leaving most of the targeting residues available.

These findings represent an asset for the future potential applications and strategies for these hybrid systems. For instance, NPs below a certain size might be transported onto (or maybe even injected into) the bacteria, exploiting the natural M13 behavior. The use of larger NPs, combined with pVIII engineering, could be exploited instead for any non-bacterial targets (in the presence of bacteria), from cancer therapy to neuro-stimulation or even to preserve bacterial cultures, exploiting the pIII inhibition (as a virus-static agent). [66, 67]

Overall, the results obtained in this work set a solid basis for the development of NP-M13 hybrid tools in a variety of applications, including (but not limited to) phage-based nanotherapeutics and nanodiagnostics. The developed methodologies, characterization platform, and workflow can be expanded to different NPs and phage types.

CONCLUSIONS

Bacteriophages are by far the most abundant biological entities present in nature. Indeed, despite their well-known potential for biotechnological and biomedical applications, they have been generally overlooked in the nanomedicine field, which could represent a revolutionizing asset.

We successfully produced a family of head-tail AuNP-M13 systems with different configurations by self-assembly, and we developed a characterization platform that allowed for a deep understanding of the NP-virus interactions. The plasmonic phages produced were stable even in complex biological fluids and presented a biomimetic behavior, eluding/minimizing biomolecular corona and exhibiting M13 biological identity, allowing for biorecognition in serum. Upon suitable M13 engineering, the AuNP-M13 could be employed in nanomedicine and sensing applications. Above all, this work sets the fundamental basis and a standard workflow for the development of phage-display-based targeting nanotools valuable for a wide spectrum of applications in different nanotechnology fields.

METHODS

M13 bacteriophages propagation and purification. The M13 phage propagation was performed as previously reported [14,15,47] (see detailed method in Supporting Information). After propagation, the incubated solutions were transferred jointly (500 mL) into a sterile ultracentrifuge tube (1 L capacity) and centrifuged at 4°C using 10000 g for 30 minutes. The pellet containing bacteria was discarded while the supernatant was transferred into another sterile ultracentrifuge tube (1 L capacity), and the centrifugation was repeated at least twice (until no *E. coli* pellet was observed). To isolate the M13 phages, PEG 6000 (20 g) / NaCl (15 g) (4% / 3% w/v) solid mixture was added to the collected supernatant, and the solution was left at 37°C under gentle shaking until the solid was completely dissolved. The mixture was then cooled in an ice bath for 30 minutes and centrifuged at 4°C using 15000 g for 30 minutes. The supernatant was discarded, and the obtained white pellet (containing the phages) was resuspended in a minimum volume of sterile H_2O (30 mL) and transferred into a polycarbonate centrifuge tube. Consequently, we employed the isoelectric point-based purification by gradually acidifying the solution, adding HCl (0.001 - 0.1 M) water solution little by little, adjusting the pH to 4.2, and inducing M13 flocculation.[48] The solution was then centrifuged at 10,000 g for 20 minutes, and the pellet (pure M13 progeny) was resuspended in sterile H_2O. The isoelectric point purification protocol was repeated at least twice, and the final pellet was resuspended in sterile PBS (pH= 7.4, 10 mM). The isolated M13 progeny was finally subjected to size exclusion chromatography (5 mL columns, Zeba spin desalting Thermofisher, 40 kDa MWCO) to remove the potential presence of small protein debris. For long-term storage, the M13 phages were kept in PBS containing 1% NaN_3 at 4°C.

Preparation of AuNPs-M13 complexes. WT-M13 bacteriophages were eluted through a 0.5 mL Zeba spin desalting column conditioned with SCS (pH= 7.0, 10 mM) for buffer exchange before reaction. Several different AuNP-M13 complexes obtained by incubating the building blocks using different stoichiometry were purified and isolated as described below:

50 nm AuNPs-M13 complexes. 50 nm AuNPs (1 nM) were diluted in SCS (1:2, pH= 7.0), M13 phages in SCS (66 nM, 4.0×10^{13} v/mL) were added using the suitable volume to achieve 1:20, 1:5, 1:1, and 5:1 (AuNPs:M13) stoichiometric equivalents, and the mixture was incubated overnight at 37°C under shaking. To isolate the 50 nm AuNPs-M13 complexes, the reaction mixture was centrifuged at 1200g for 25 minutes to precipitate unreacted 50 nm AuNPs (no pellet was found when using M13 large excess). The supernatant was collected, transferred into a protein LoBind tube, and centrifuged at 10000 g for 30 minutes. The colorless supernatant containing free M13 was discarded, and the pellet (50 nm AuNPs-M13) was resuspended in SCS. This washing step was repeated multiple times to ensure the absence of free M13 phages (verified by SDS-PAGE silver staining). The samples were stored at 4°C and used within two weeks.

15 nm and 5 nm AuNPs-M13 complexes were prepared similarly with an adapted purification protocol. The detailed methods description is reported in Supporting Information.

The methods related to the characterization of the complexes are detailed in Supporting Information.

Direct analysis (without workup) of the interactions between M13s and AuNPs were also performed by DCS (see Differential Centrifugal Sedimentation section for experimental details in Supporting Informations).

DCS Mathematical Model. We considered a hybrid system of N_0 spherical NP of diameter d_0 and density ρ_0, attached to N_f filaments (M13 phages) of length L, diameter d_f, and density ρ_f. The NP and filament volumes are $V_0 = d_0^3/6\pi$, and $V_f = d_f^2\, L/4\pi$, respectively, and the total volume of the hybrid system is $V = N_0V_0 + N_fV_f$. The density as a whole will be given by the weighted average:

$$\rho = \frac{N_0\rho_0\, V_0 \; + \; N_f\rho_f\, V_f}{V}.$$

The magnitude of the terminal velocity U of the object is proportional to the magnitude of the external force applied to the object: $F = Va(\rho - \rho_w)$, where a is the centrifugal acceleration and ρ_w the average density of the sucrose gradient. The proportionality factor is given by the inverse of the drag coefficient.

For a sphere, we have $U_0 = F_0/c_0$, with the drag coefficient $c_0 = 3\pi\mu d_0$.

For a slender filament the drag coefficient depends on its orientation with respect to direction of motion.[68] If the velocity of the filament relative to the fluid is parallel to the filament, we have $U_{\parallel} = F/c_{\parallel}$, with:

$$c_{\parallel} = \frac{4\pi\mu L}{ln(4\epsilon^{-2}) - 1};$$

and for the velocity perpendicular to the filament $U_{\perp} = \mathrm{F}/c_{\perp}$, we have

$$c_{\perp} = \frac{8\pi\mu L}{ln(4\epsilon^{-2}) + 1}.$$

The parameter $\epsilon = d_f/L$ is the slenderness parameter. Note that as far as $L \gg d_f$, the results do not depend much on the exact value of ϵ.

We assume that the total drag coefficient of the overall object (NPs + attached filaments) is the sum of the drag coefficients of the N_0 spherical NPs and the N_f filaments. The terminal velocity of the overall object (NPs + filaments), relative to the velocity of a single NP is:

$$U_{\parallel}/U_0 = \frac{V(\rho - \rho_w)}{V_0(\rho_0 - \rho_w)} \frac{c_0}{N_f\, c_{\parallel} + N_0 c_0},$$

$$U_{\perp}/U_0 = \frac{V(\rho - \rho_w)}{V_0(\rho_0 - \rho_w)} \frac{c_0}{N_f\, c_{\perp} + N_0 c_0},$$

for the parallel and perpendicular configuration, respectively.

In practice, we obtain excellent data fitting by assuming filaments are orientated in random directions and averaging results for the perpendicular and parallel configurations. Therefore, we only present results obtained with the average $c_f = (c_{\perp} + c_{\parallel})/2$ as drag coefficient for a filament. Repeating calculations for several values of d_0 within the measured distribution of the particle diameter, we can estimate the distribution of the sedimentation times for a specific composition of the system (that is, specific values of N_0 and N_f, e.g. **Figure 3C** lower panel).

For the analysis of a mixed polulation, we estimated the percentage of each complex configuration N_0AuNP: N_fM13 by fitting the distribution of measured sedimentation times (e.g. **Figure 3D,E**).

Computational simulations. The calculation of the adsorption energies is based on the previously reported multiscale approach [61,68] and, in the following paragraph, we present a brief description of the methodology. In this model, the crystal structures of the different components of the M13 protein are used as the starting point. Based on this information, a protein is represented by a set of beads, whose centers are placed at the position of the α-carbon atoms. In this way, the model has a resolution of one bead per residue. In the case of the nanoparticles, each of them is represented by a single bead. With the protein and NP model defined, the next step is to define the interaction between each of the 20 amino acids and the NP. For this, we assume that the total protein-NP interaction energy (which is a function of the separation between the protein and the NP) is made of the sum of energies of non-bonded (van der Waals) and electrostatic interactions between all amino acids and the NP. Notice that in this approximation, the proteins are treated as being rigid. The van der Waals interaction term is composed of two contributions: the surface of the NP, which is obtained from all-atom simulations, and the core of the NP, which is approximated by a continuum model based on Lifshitz theory. The electrostatic interaction is approximated by a Debye-Huckel potential.

The calculation of the adsorption energy is then performed for different orientations of the protein facing the NP surface. For this, points on the surface of the proteins are defined, and the total interaction energy as a function of the distance between the NP and the protein is calculated and used to obtain the adsorption energy for each of these points (orientations). A weighted Boltzmann average is calculated to obtain the overall adsorption energy. [61,69]

Plaque Assay. The plaque assays were performed by modifying slightly a previously reported protocol.[70] Briefly, 5 mL LB media was inoculated in a 50 mL sterile culture tube (pyrogen-free falcon) with an *E. coli* (TG1 strain) isolated single colony picked from a streaked culture on an agar plate. After 4-5 hours in a rotatory shaker at 37°C (250 rpm), the bacterial suspension should reach $0.4 > OD_{600nm} < 0.6$. Separately, 3 mL of melted soft agar (0.7% w/v) was prepared using LB medium (supplemented by 0.02% IPTG (v/v)) and kept in a 15 mL sterile tube inside a water bath at 50°C (melted top agar). To a 400 µL of bacterial culture, 20 µL of M13 phages / AuNPs-M13 complex (normalized at $4x10^3$ v/mL) were added and vortexed gently. 300 µL of this mixture were transferred into the top agar tube, vortexed gently, and rapidly added to a 100 mm x 15 mm hard 1.5 % agar plate prepared with LB culture media. The plates were then incubated statically overnight at 37°C. The experiments were also performed using multiple dilutions with all samples M13 phages, 5 nm AuNPs-M13, 15 nm AuNPs-M13, and 50 nm AuNPs-M13 to obtain the optimized conditions. The Plaque Forming Units were counted using ImageJ software.

ASSOCIATED CONTENT

Supporting Information. The Supporting Information file containing the following data is available free of charge as PDF. Supporting Figures, a supplementary detailed Materials and Methods section, additional results on the characterization of M13s, AuNPs and AuNP-M13s including TEM micrographs, absorption spectra and DLS meaurments together with additional data related to the AuNP-M13 interactions, AuNP-M13 interaction with proteins, and their stability in biological media, gel-electrophoresis, immunoblotting assays, DCS analysis, plaque tests and in silico experiments.

AUTHOR INFORMATION

Corresponding Author

*Luca Boselli (luca.boselli@iit.it), * Pier Paolo Pompa (pierpaolo.pompa@iit.it)

Funding Sources

ERA-NET Joint Programme for Neurodegenerative Disease 2020 under the Neurophage grant (ER-2020-23669249); Michael J. Fox Foundation under the PhageTrigger grant (MJFF-021697); “Roche per la Ricerca” under the NeuroTarget grant; Italian Ministry of University and Research (MUR) under the PRIN2020 (2020WMSNBL), and PRIN2022 (2022A5YWJJ).

ACKNOWLEDGMENT

VC and FB thank ERA-NET Joint Programme for Neurodegenerative Disease 2020 under the Neurophage grant (ER-2020-23669249), the Michael J. Fox Foundation under the PhageTrigger grant (MJFF-021697), and “Roche per la Ricerca” under the NeuroTarget grant. AD and FB thank the Italian Ministry of University and Research (MUR) under the PRIN2020 (2020WMSNBL), and PRIN2022 (2022A5YWJJ). PPP and LB thank the IIT EM-facility. The authors wish to acknowledge the Irish Centre for High-End Computing (ICHEC) for the provision of computational facilities and support.

REFERENCES

1. Gray, A.; Bradbury, A. R.; Knappik, A.; Plückthun, A.; Borrebaeck, C. A.; Dübel, S., Animal-free alternatives and the antibody iceberg. *Nature Biotechnology* **2020,** *38* (11), 1234-1239.

2. Xu, J.; Miao, H.; Wang, J.; Pan, G., Molecularly imprinted synthetic antibodies: from chemical design to biomedical applications. *Small* **2020,** *16* (27), 1906644.

3. Li, K.; Chen, Y.; Li, S.; Nguyen, H. G.; Niu, Z.; You, S.; Mello, C. M.; Lu, X.; Wang, Q., Chemical modification of M13 bacteriophage and its application in cancer cell imaging. *Bioconjugate chemistry* **2010,** *21* (7), 1369-1377.

4. Singh, A.; Arutyunov, D.; Szymanski, C. M.; Evoy, S., Bacteriophage based probes for pathogen detection. *Analyst* **2012,** *137* (15), 3405-3421.

5. Smith, G. P.; Petrenko, V. A., Phage display. *Chemical reviews* **1997,** *97* (2), 391-410.

6. Pande, J.; Szewczyk, M. M.; Grover, A. K., Phage display: concept, innovations, applications and future. *Biotechnology advances* **2010,** *28* (6), 849-858.

7. Jaroszewicz, W.; Morcinek-Orłowska, J.; Pierzynowska, K.; Gaffke, L.; Węgrzyn, G., Phage display and other peptide display technologies. *FEMS Microbiology Reviews* **2022,** *46* (2), fuab052.

8. Barr, J. J., A bacteriophages journey through the human body. *Immunological Reviews* **2017,** *279* (1), 106-122.

9. Garretto, A.; Miller-Ensminger, T.; Wolfe, A. J.; Putonti, C., Bacteriophages of the lower urinary tract. *Nature Reviews Urology* **2019,** *16* (7), 422-432.

10. Górski, A.; Ważna, E.; Dąbrowska, B.-W.; Dąbrowska, K.; Świtała-Jeleń, K.; Międzybrodzki, R., Bacteriophage translocation. *FEMS Immunology & Medical Microbiology* **2006,** *46* (3), 313-319.

11. Tetz, G.; Tetz, V., Bacteriophages as new human viral pathogens. *Microorganisms* **2018,** *6* (2), 54.

12. Harada, L. K.; Silva, E. C.; Campos, W. F.; Del Fiol, F. S.; Vila, M.; Dąbrowska, K.; Krylov, V. N.; Balcão, V. M., Biotechnological applications of bacteriophages: State of the art. *Microbiological research* **2018,** *212*, 38-58.

13. Peltomaa, R.; Lopez-Perolio, I.; Benito-Pena, E.; Barderas, R.; Moreno-Bondi, M. C., Application of bacteriophages in sensor development. *Analytical and bioanalytical chemistry* **2016,** *408*, 1805-1828.

14. Ulfo, L.; Cantelli, A.; Petrosino, A.; Costantini, P. E.; Nigro, M.; Starinieri, F.; Turrini, E.; Zadran, S. K.; Zuccheri, G.; Saporetti, R., Orthogonal nanoarchitectonics of M13 phage for receptor targeted anticancer photodynamic therapy. *Nanoscale* **2022,** *14* (3), 632-641.

15. Petrosino, A.; Saporetti, R.; Starinieri, F.; Sarti, E.; Ulfo, L.; Boselli, L.; Cantelli, A.; Morini, A.; Zadran, S. K.; Zuccheri, G., A modular phage vector platform for targeted photodynamic therapy of Gram-negative bacterial pathogens. *Iscience* **2023,** *26* (10).

16. Kim, J.; Adhikari, M.; Dhamane, S.; Hagström, A. E.; Kourentzi, K.; Strych, U.; Willson, R. C.; Conrad, J. C., Detection of viruses by counting single fluorescent genetically biotinylated reporter immunophage using a lateral flow assay. *ACS applied materials & interfaces* **2015,** *7* (4), 2891-2898.

17. Chabi, M.; Vu, B.; Brosamer, K.; Smith, M.; Chavan, D.; Conrad, J. C.; Willson, R. C.; Kourentzi, K., Smartphone-read phage lateral flow assay for point-of-care detection of infection. *Analyst* **2023,** *148* (4), 839-848.

18. Farooq, U.; Yang, Q.; Ullah, M. W.; Wang, S., Bacterial biosensing: Recent advances in phage-based bioassays and biosensors. *Biosensors and Bioelectronics* **2018,** *118*, 204-216.

19. Conners, R.; León-Quezada, R. I.; McLaren, M.; Bennett, N. J.; Daum, B.; Rakonjac, J.; Gold, V. A., Cryo-electron microscopy of the f1 filamentous phage reveals insights into viral infection and assembly. *Nature Communications* **2023,** *14* (1), 2724.

20. Han, S. M.; Lee, Y. J.; Lee, M. H.; Park, C. W.; Lee, S. M.; Soh, J. O.; Lee, J. H., M13 Bacteriophage-Based Bio-nano Systems for Bioapplication. *BioChip Journal* **2022,** *16* (3), 227-245.

21. Zhou, X.; Cao, P.; Zhu, Y.; Lu, W.; Gu, N.; Mao, C., Phage-mediated counting by the naked eye of miRNA molecules at attomolar concentrations in a Petri dish. *Nature materials* **2015,** *14* (10), 1058-1064.

22. Xu, H.; Shen, J.; Yang, C.-T.; Thierry, B.; Zhu, Y.; Mao, C.; Zhou, X., Naked-eye counting of pathogenic viruses by phage-gold nanobiomaterials as probes. *Materials Today Advances* **2021,** *10*, 100122.

23. Hou, J.; Xu, Y.; Sun, S.; Zhong, X.; Yang, C.-T.; Zhou, X., Gold nanoparticles-decorated M13 phage SPR probe for dual detection of antigen biomarkers in serum. *Sensors and Actuators B: Chemical* **2023,** *374*, 132811.

24. Alarcón-Correa, M.; Günther, J.-P.; Troll, J.; Kadiri, V. M.; Bill, J.; Fischer, P.; Rothenstein, D., Self-assembled phage-based colloids for high localized enzymatic activity. *ACS nano* **2019,** *13* (5), 5810-5815.

25. Ghosh, D.; Lee, Y.; Thomas, S.; Kohli, A. G.; Yun, D. S.; Belcher, A. M.; Kelly, K. A., M13-templated magnetic nanoparticles for targeted in vivo imaging of prostate cancer. *Nature nanotechnology* **2012,** *7* (10), 677-682.

26. Yi, H.; Ghosh, D.; Ham, M.-H.; Qi, J.; Barone, P. W.; Strano, M. S.; Belcher, A. M., M13 phage-functionalized single-walled carbon nanotubes as nanoprobes for second near-infrared window fluorescence imaging of targeted tumors. *Nano letters* **2012,** *12* (3), 1176-1183.

27. Urquhart, T.; Daub, E.; Honek, J. F., Bioorthogonal modification of the major sheath protein of bacteriophage M13: extending the versatility of bionanomaterial scaffolds. *Bioconjugate Chemistry* **2016,** *27* (10), 2276-2280.

28. Szot-Karpińska, K.; Golec, P.; Leśniewski, A.; Pałys, B.; Marken, F.; Niedziółka-Jönsson, J.; Węgrzyn, G.; Łoś, M., Modified filamentous bacteriophage as a scaffold for carbon nanofiber. *Bioconjugate Chemistry* **2016,** *27* (12), 2900-2910.

29. Chung, W.-J.; Lee, D.-Y.; Yoo, S. Y., Chemical modulation of M13 bacteriophage and its functional opportunities for nanomedicine. *International journal of nanomedicine* **2014**, 5825-5836.

30. Peng, H.; Chen, I. A., Rapid colorimetric detection of bacterial species through the capture of gold nanoparticles by chimeric phages. *Acs Nano* **2018,** *13* (2), 1244-1252.

31. Boselli, L.; Castagnola, V.; Armirotti, A.; Benfenati, F.; Pompa, P. P., Biomolecular Corona of Gold Nanoparticles: The Urgent Need for Strong Roots to Grow Strong Branches. *Small* **2023**, 2306474.

32. Cai, Q.; Castagnola, V.; Boselli, L.; Moura, A.; Lopez, H.; Zhang, W.; de Araújo, J. M.; Dawson, K. A., A microfluidic approach for synthesis and kinetic profiling of branched gold nanostructures. *Nanoscale Horizons* **2022,** *7* (3), 288-298.

33. Boselli, L.; Lopez, H.; Zhang, W.; Cai, Q.; Giannone, V. A.; Li, J.; Moura, A.; de Araujo, J. M.; Cookman, J.; Castagnola, V., Classification and biological identity of complex nano shapes. *Communications Materials* **2020,** *1* (1), 35.

34. Eustis, S.; El-Sayed, M. A., Why gold nanoparticles are more precious than pretty gold: noble metal surface plasmon resonance and its enhancement of the radiative and nonradiative properties of nanocrystals of different shapes. *Chemical society reviews* **2006,** *35* (3), 209-217.

35. Loynachan, C. N.; Soleimany, A. P.; Dudani, J. S.; Lin, Y.; Najer, A.; Bekdemir, A.; Chen, Q.; Bhatia, S. N.; Stevens, M. M., Renal clearable catalytic gold nanoclusters for in vivo disease monitoring. *Nature nanotechnology* **2019,** *14* (9), 883-890.

36. Liu, C. P.; Wu, T. H.; Liu, C. Y.; Chen, K. C.; Chen, Y. X.; Chen, G. S.; Lin, S. Y., Self-supplying O2 through the catalase-like activity of gold nanoclusters for photodynamic therapy against hypoxic cancer cells. *Small* **2017,** *13* (26), 1700278.

37. Xu, D.; Wu, L.; Yao, H.; Zhao, L., Catalase-Like Nanozymes: Classification, Catalytic Mechanisms, and Their Applications. *Small* **2022,** *18* (37), 2203400.

38. Zhang, W.; Lopez, H.; Boselli, L.; Bigini, P.; Perez-Potti, A.; Xie, Z.; Castagnola, V.; Cai, Q.; Silveira, C. P.; de Araujo, J. M., A nanoscale shape-discovery framework supporting systematic investigations of shape-dependent biological effects and immunomodulation. *ACS nano* **2021,** *16* (1), 1547-1559.

39. Talamini, L.; Violatto, M. B.; Cai, Q.; Monopoli, M. P.; Kantner, K.; Krpetic, Z.; Perez-Potti, A.; Cookman, J.; Garry, D.; Silveira, C. P., Influence of size and shape on the anatomical distribution of endotoxin-free gold nanoparticles. *ACS nano* **2017,** *11* (6), 5519-5529.

40. Boisselier, E.; Astruc, D., Gold nanoparticles in nanomedicine: preparations, imaging, diagnostics, therapies and toxicity. *Chemical society reviews* **2009,** *38* (6), 1759-1782.

41. Dreaden, E. C.; Alkilany, A. M.; Huang, X.; Murphy, C. J.; El-Sayed, M. A., The golden age: gold nanoparticles for biomedicine. *Chemical Society Reviews* **2012,** *41* (7), 2740-2779.

42. Singh, P.; Pandit, S.; Mokkapati, V.; Garg, A.; Ravikumar, V.; Mijakovic, I., Gold nanoparticles in diagnostics and therapeutics for human cancer. *International journal of molecular sciences* **2018,** *19* (7), 1979.

43. Peng, H.; Borg, R. E.; Dow, L. P.; Pruitt, B. L.; Chen, I. A., Controlled phage therapy by photothermal ablation of specific bacterial species using gold nanorods targeted by chimeric phages. *Proceedings of the National Academy of Sciences* **2020,** *117* (4), 1951-1961.

44. Huang, Y.; Chiang, C.-Y.; Lee, S. K.; Gao, Y.; Hu, E. L.; Yoreo, J. D.; Belcher, A. M., Programmable assembly of nanoarchitectures using genetically engineered viruses. *Nano letters* **2005,** *5* (7), 1429-1434.

45. Slot, J.W.; H.J. Geuze; A new method of preparing gold probes for multiple-labeling cytochemistry. *European journal of cell biology* **1985,** 38 (1), 87-93.

46. Grzelczak, M.; Pérez-Juste, J.; Mulvaney, P.; Liz-Marzán, L. M., Shape control in gold nanoparticle synthesis. *Colloidal Synthesis of Plasmonic Nanometals* **2020**, 197-220.

47. Bortot, B.; Apollonio, M.; Baj, G.; Andolfi, L.; Zupin, L.; Crovella, S.; di Giosia, M.; Cantelli, A.; Saporetti, R.; Ulfo, L., Advanced photodynamic therapy with an engineered M13 phage targeting EGFR: Mitochondrial localization and autophagy induction in ovarian cancer cell lines. *Free Radical Biology and Medicine* **2022,** *179*, 242-251.

48. Passaretti, P.; Khan, I.; Dafforn, T. R.; Goldberg Oppenheimer, P., Improvements in the production of purified M13 bacteriophage bio-nanoparticle. *Scientific Reports* **2020,** *10* (1), 18538.

49. Passaretti, P.; Sun, Y.; Dafforn, T. R.; Oppenheimer, P. G., Determination and characterisation of the surface charge properties of the bacteriophage M13 to assist bio-nanoengineering. *RSC advances* **2020,** *10* (42), 25385-25392.

50. Branston, S.; Stanley, E.; Keshavarz-Moore, E.; Ward, J., Precipitation of filamentous bacteriophages for their selective recovery in primary purification. *Biotechnology progress* **2012,** *28* (1), 129-136.

51. Morag, O.; Sgourakis, N. G.; Abramov, G.; Goldbourt, A., Filamentous bacteriophage viruses: preparation, magic-angle spinning solid-state nmr experiments, and structure determination. *Protein NMR: Methods and Protocols* **2018**, 67-97.

52. Kostrikis, L. G.; Liu, D. J.; Day, L. A., Ultraviolet absorbance and circular dichroism of Pf1 virus: nucleotide/subunit ratio of unity, hyperchromic tyrosines and DNA bases, and high helicity in the subunits. *Biochemistry* **1994,** *33* (7), 1694-1703.

53. Tarricone, G.; Castagnola, V.; Mastronardi, V.; Cursi, L.; Debellis, D.; Ciobanu, D. Z.; Armirotti, A.; Benfenati, F.; Boselli, L.; Pompa, P. P., Catalytic Bioswitch of Platinum Nanozymes: Mechanistic Insights of Reactive Oxygen Species Scavenging in the Neurovascular Unit. *Nano Letters* **2023**.

54. Donati, P.; Pomili, T.; Boselli, L.; Pompa, P. P., Colorimetric nanoplasmonics to spot hyperglycemia from saliva. *Frontiers in bioengineering and biotechnology* **2020,** *8*, 601216.

55. Monopoli, M. P.; Aberg, C.; Salvati, A.; Dawson, K. A., Biomolecular coronas provide the biological identity of nanosized materials. *Nano-enabled medical applications* **2020**, 205-229.

56. Dawson, K. A.; Yan, Y., Current understanding of biological identity at the nanoscale and future prospects. *Nature nanotechnology* **2021,** *16* (3), 229-242.

57. Perez-Potti, A.; Lopez, H.; Pelaz, B.; Abdelmonem, A.; Soliman, M. G.; Schoen, I.; Kelly, P. M.; Dawson, K. A.; Parak, W. J.; Krpetic, Z., In depth characterisation of the biomolecular coronas of polymer coated inorganic nanoparticles with differential centrifugal sedimentation. *Scientific Reports* **2021,** *11* (1), 6443.

58. Walczyk, D.; Bombelli, F. B.; Monopoli, M. P.; Lynch, I.; Dawson, K. A., What the cell “sees” in bionanoscience. *Journal of the American Chemical Society* **2010,** *132* (16), 5761-5768.

59. Krpetic, Z.; Davidson, A. M.; Volk, M.; Levy, R.; Brust, M.; Cooper, D. L., High-resolution sizing of monolayer-protected gold clusters by differential centrifugal sedimentation. *Acs Nano* **2013,** *7* (10), 8881-8890.

60. Ke, P. C.; Lin, S.; Parak, W. J.; Davis, T. P.; Caruso, F., A decade of the protein corona. *ACS nano* **2017,** *11* (12), 11773-11776.

61. Power, D.; Rouse, I.; Poggio, S.; Brandt, E.; Lopez, H.; Lyubartsev, A.; Lobaskin, V., A multiscale model of protein adsorption on a nanoparticle surface. *Modelling and Simulation in Materials Science and Engineering* **2019,** *27* (8), 084003.

62. Simonelli, F.; Rossi, G.; Monticelli, L., Role of ligand conformation on nanoparticle–protein interactions. *The Journal of Physical Chemistry B* **2019,** *123* (8), 1764-1769.

63. Jumper, J.; Evans, R.; Pritzel, A.; Green, T.; Figurnov, M.; Ronneberger, O.; Tunyasuvunakool, K.; Bates, R.; Žídek, A.; Potapenko, A., Highly accurate protein structure prediction with AlphaFold. *Nature* **2021,** *596* (7873), 583-589.

64. Holliger, P.; Riechmann, L.; Williams, R. L., Crystal structure of the two N-terminal domains of g3p from filamentous phage fd at 1.9 Å: evidence for conformational lability. *Journal of molecular biology* **1999,** *288* (4), 649-657.

65. Lubkowski, J.; Hennecke, F.; Plückthun, A.; Wlodawer, A., The structural basis of phage display elucidated by the crystal structure of the N-terminal domains of g3p. *Nature structural biology* **1998,** *5* (2), 140-147.

66. Richter, Ł.; Paszkowska, K.; Cendrowska, U.; Olgiati, F.; Silva, P. J.; Gasbarri, M.; Guven, Z. P.; Paczesny, J.; Stellacci, F., Broad-spectrum nanoparticles against bacteriophage infections. *Nanoscale* **2021,** *13* (44), 18684-18694.

67. Richter, Ł.; Stevens, C. A.; Silva, P. J.; Julià, L. R.; Malinverni, C.; Wei, L.; Łoś, M.; Stellacci, F., Peptide-grafted nontoxic cyclodextrins and nanoparticles against bacteriophage infections. *ACS nano* **2022,** *16* (11), 18990-19001.

68. Lighthill, J. Flagellar hydrodynamics. *SIAM review* **1976,** *18*(2), 161-230.

69. Lopez, H.; Lobaskin, V. Coarse-grained model of adsorption of blood plasma proteins onto nanoparticles. *Journal of Chemical Physics* **2015,** *143*, 24.

70. Green, M. R. & Sambrook, J. Plating Bacteriophage M13. *Cold Spring Harb Protocols* **2017**, *10*, pdb.prot093427.

Citation on deposit: Ahmed, H., Lopez, H., Boselli, F., Tarricone, G., Vercellino, S., Costantini, P. E., Castagnola, V., Veronesi, M., Benfenati, F., Danielli, A., Boselli, L., & Pompa, P. P. (2024). Biomimetic Plasmonic Nanophages by Head/Tail Self-Assembling: Gold Nanoparticle/Virus Interactions. ACS Nano, 18(32), 21302-21315. https://doi.org/10.1021/acsnano.4c05198